Energy 346 (2026) 140188

Contents lists available at ScienceDirect

Energy

journal homepage: www.elsevier.com/locate/energy

An integrated degradation-aware framework for sizing and energy management in hybrid multi-stack fuel cell vehicles

Hamid Bakhshi Yamchi [a,*], Mohammadreza Moghadari [a], Mohsen Kandidayeni [a], Sousso Kelouwani [b], Loïc Boulon [a]

[a] Hydrogen Research Institute, Department of Electrical and Computer Engineering, Université Du Québec à Trois-Rivières, QC, G8Z 4M3, Canada
[b] Department of Mechanical Engineering, Faculty of Engineering, Université Du Québec à Trois-Rivières, QC, G8Z 4M3, Canada

ARTICLE INFO

Keywords:
Proton exchange membrane fuel cell
Design–operation integrated framework
Multi-objective optimization
Modular fuel cell system
Degradation-aware optimization
Heavy-duty vehicles

ABSTRACT

This paper proposes a degradation-aware integrated sizing and energy management strategy (ISEMS) for hybrid multi-stack fuel cell systems (MFCSs) in heavy-duty vehicles (HDVs), aiming to minimize total cost while enhancing system durability. While ISEMS approaches have been explored for single-stack systems, their extension to MFCSs remains unexplored. The proposed method simultaneously determines the size of the fuel cell (FC) stacks and the battery configuration, and evaluates the performance of the system under different FC stack arrangements. Unlike conventional approaches, sizing and stack allocation are handled jointly, without assuming a fixed total FC capacity. The degradation behavior of both the FC stacks and the battery is embedded in both sizing and energy management stages to improve system longevity. A hybrid genetic algorithm–model predictive control (GA–MPC) framework is employed, where GA explores design configurations and MPC ensures degradation-aware power allocation. The method is validated in a long-haul truck case study, where ISEMS reduces total cost by 68 % and 50 % compared to single-stack and quad-stack configurations from previous studies. Experimental validation is also conducted using data from FCs installed on a multi-stack test bench, in order to identify their optimal arrangement with the proposed method. Sensitivity analyses also demonstrate that widening the battery state of charge (SOC) window leads to additional cost reductions of up to 67.4 % by enhancing battery utilization. The proposed framework offers a scalable, degradation-aware solution for cost-effective MFCS design and control in HDV applications.

1. Introduction

The transportation sector uses 25 % of the world's energy, relying mainly on fossil fuels and making a significant contribution to climate change [1]. While hybrid and battery electric vehicles (HEVs and BEVs) support cleaner transport, BEVs face major limitations for heavy-duty vehicles (HDVs), including short range, insufficient charging infrastructure, and bulky battery systems [2,3].

Hydrogen is a promising energy source, with global demand projected to reach 1370 MMT by 2050, up to 33.1 % of which may come from transportation [4,5]. Vehicles using fuel cells (FCs), particularly for HDVs, benefit from hydrogen's high energy density and fast refueling. Proton exchange membrane fuel cells (PEMFCs) are the most used in vehicles due to their low operating temperature, high power density, and compact, safe design [6]. However, PEMFCs face limitations like slow response and cold starts. To overcome these, energy storage systems (ESSs) such as batteries and supercapacitors are integrated to enhance performance, protect the FC, and recover energy [7]. PEMFC-battery configurations are widely adopted in fuel cell hybrid electric vehicles (FC-HEVs) to ensure dynamic power support and system reliability [8].

While FC technology has matured for light-duty vehicles (LDVs) over the past two decades, its application to HDVs has gained interest more recently. A key advantage is reduced infrastructure needs, as HDVs often follow fixed routes, minimizing refueling station requirements [9]. High-power single-stack FC systems (FCSs) have been widely used in FC-HEV powertrains [10–12], but their output is insufficient for HDVs. Consequently, research is shifting toward multi-stack FC systems (MFCSs), which combine independent stacks to meet higher power demands. MFCSs offer advantages in power scalability, reliability, and spatial flexibility [13]. They also enhance modularity and adaptability across varying operational needs. However, managing multiple stacks

* Corresponding author.
E-mail address: hamid.bakhshi.yamchi@uqtr.ca (H.B. Yamchi).

https://doi.org/10.1016/j.energy.2026.140188
Received 27 August 2025; Received in revised form 17 December 2025; Accepted 24 January 2026
Available online 27 January 2026

Table 1
Summary and comparison of literature focusing on power source sizing and EMSs for FC-HEVs.

Ref.	FC sizing	Battery sizing	EMS	Multi-stack	Stack allocation	FC count Analysis
[17–20]	✓	✓	×	×	×	×
[21–23, 25–36, 50–52]	×	×	✓	✓	×	×
[37,38]	×	×	✓	×	×	×
[40–45]	✓	✓	✓	×	×	×
[46]	✓	×	✓	✓	×	×
[47–49]	×	×	✓	✓	✓	✓
This study	✓	✓	✓	✓	✓	✓

and an ESS creates system complexity, requiring careful sizing and a robust energy management strategy (EMS) to fully exploit MFCS capabilities.

Accurate sizing of the FC and battery is essential in FC-HEVs to ensure that power demands are reliably met while avoiding excess weight and cost [14]. Undersizing impairs load supply, whereas oversizing increases weight and cost, potentially reducing appeal [15]. This is particularly crucial for HDVs, where high power demand and durability necessitate precise sizing for feasibility and cost-efficiency [16]. Prior studies have addressed this [17]: proposed an FC-HEV outperforming the first-gen Toyota Mirai in gradeability and reducing power source cost by 28 % [18]; found that in FC/battery buses, battery-dominant setups reduced degradation and lifetime costs [19]; studied FC-hybrid trains using real locomotive data, showing higher battery-to-FC ratios; and [20] developed a sizing method for FC trucks, concluding that while batteries are currently cheaper, FCs may offer long-term economic benefits.

The EMS manages power distribution to follow the powertrain power request whilst minimizing hydrogen use and system degradation, and is typically classified as rule-based, optimization-based, or intelligent [21]. Rule-based EMSs are simple and efficient but rely on empirical tuning, limiting optimality [22,23]. Optimization-based EMSs define an objective function with constraints to minimize it [24]. Dynamic programming (DP) has been used for offline global optimization in FC systems [25–27], but its application in MFCSs is limited due to computational complexity. Even as a benchmark [28], DP is often simplified and lacks health awareness. To address this, the authors of [29] proposed the Constrained Exploration Method (CEM), which uses filters to reduce DP's computational burden. This method was also adopted in an aviation-focused study to evaluate the performance of single- and multi-stack FC configurations [30]. Online methods have also been proposed for real-time use. For example [31,32], introduced hierarchical EMSs [33], extended ECMS to multi-stack and aircraft applications, while [34,35] developed strategies for trams and modular FCs, and [36] introduced a predictive EMS combining rule-based control and MPC. Although suitable for real-time application, these online approaches typically optimize over short horizons. More recently, advanced intelligent strategies such as deep reinforcement learning have been applied to FC buses to integrate future road information with cabin comfort control [37], while other health-conscious frameworks have demonstrated that coupling thermal management of the cabin and energy sources can significantly enhance system durability [38].

Some studies have shown that separating sizing and EMS design can reduce performance and increase energy storage costs, emphasizing the need for joint or integrated optimization [39]. Since component sizes constrain FCS operation, sizing directly influences EMS performance. Joint optimization of sizing and EMS enhances durability, cost-efficiency, and overall system effectiveness. However, these studies have primarily focused on single-stack FCSs, without addressing multi-stack configurations. In Ref. [40], a method based on Toyota Mirai data and MATLAB-SIMULINK modeling was proposed to optimize component sizing and power distribution, prolonging FC durability and reducing fuel consumption. In Ref. [41], integrated modeling, sizing, and EMS using tunnel DP and Pareto analysis reduced operational cost in FC-HEVs. Study [42] showed that slightly undersized FCs with well-tuned EMSs offered optimal trade-offs in consumption, degradation, and cost. In Ref. [43], DP-based sizing for FC-battery excavators showed that increasing the number of FC cells led to reduced hydrogen consumption and better SOC sustainability, while excessive sizing adversely affected battery performance. A hybrid ESS with an adaptive-weight genetic algorithm enhanced range and extended component life in Ref. [44]. Lastly [45], proposed a cost-effective sizing method using chance-constrained optimization, evaluating three ESS types across HDV applications with FC degradation considerations.

However, the impact of stack number and sizing on MFCS performance has often been overlooked, despite their significant influence on both capital and operational costs. While a higher number of stacks allows the EMS to manage power more flexibly and potentially reduce degradation and hydrogen use, allowing for unequal rated powers introduces many possible configurations, each with different cost and performance implications. In Ref. [46], modular FC configurations with differential control improved durability and reduced total ownership cost and emissions by up to 23 %, though the analysis was limited to three dual-stack setups. The authors of [47,48] proposed two optimization methods for MFCSs in HDVs [47]: used bi-level optimization to enhance efficiency and RUL, while [48] extended it to a multi-objective framework minimizing cost and maximizing durability. Both studies confirmed performance gains and hydrogen savings over equal-stack setups. In Ref. [49], SQP-based EMS was used to optimize stack allocation, showing that increasing the number of stacks from two to three and from three to four reduced operational costs by 6.33 % and 14.87 %, respectively. These studies developed multi-stack configurations based on predefined single-stack sizing, highlighting the critical role of appropriate stack allocation in minimizing FCS costs.

To provide a concise synthesis, Table 1 categorizes the scope of the relevant studies. This analysis clearly highlights the persistent research gap regarding the integrated optimization of component sizing and EMS for MFCSs.

To the best of our knowledge, existing studies have not addressed sizing and EMS for reducing investment and operational costs in MFCSs. Some explore finite configurations or focus on stack allocation with fixed total FCS size, often overlooking battery sizing. This leaves a gap in integrated approaches to sizing, stack allocation, and EMS. To fill this, an optimization-based framework called the Integrated Sizing and Energy Management Strategy (ISEMS) is proposed, which jointly determines FC and battery sizes to minimize total cost. The total cost includes both investment and operational costs. The investment cost accounts for the expenses associated with FC systems, battery, and power converters, while the operation expense reflects the cost of hydrogen usage as well as the degradation costs of FC stacks and the battery. Unlike prior works that fix FC size before allocation, the proposed approach unifies stack sizing and allocation, and analyzes how the number of stacks affects investment and operational costs. The SOH constraints have been also added into the formulation to improve system durability. Therefore, the main contributions of this study can be summarized as follows.

- An optimization-based method is developed to simultaneously address ISEMS in MFCSs, with the goal of minimizing both operational and investment costs.
- The sizing and allocation of FC stacks are treated as a single integrated process, rather than being handled separately with a predefined total FC size.
- Joint determination of battery size and FC configuration, with SOH considerations included to ensure a integrated and durable system design.

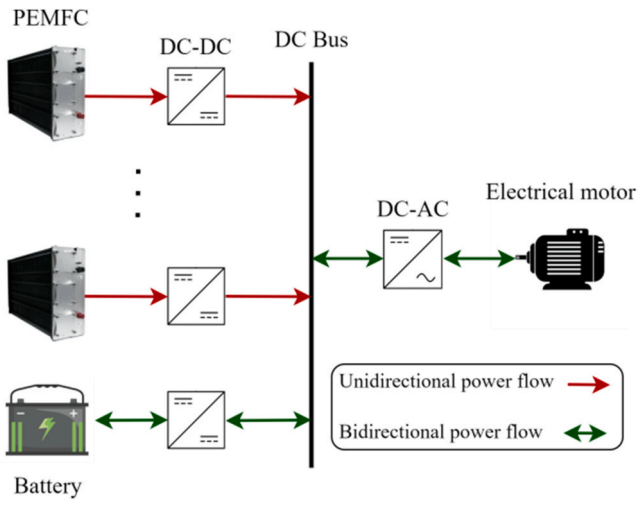

Fig. 1. The configuration of an MFCS powertrain.

Table 2
Coefficients related to FC degradation.

Coefficient	Value
k_s	1.379×10^{-3} $\left(\%.\ cycle^{-1}\right)$
k_f	4.41×10^{-9} $\left(\%.\ W^{-1}\right)$
k_l	8.662×10^{-4} $\left(\%.\ h^{-1}\right)$
k_h	10^{-3} $\left(\%.\ h^{-1}\right)$

- Optimal FC system sizes are identified for different numbers of FC stacks, and the impact of stack quantity on both investment and operational costs is analyzed.

The remainder of this paper is structured as follows: Section 2 presents system modeling; Section 3 details the ISEMS method; Section 4 reports simulation results; and Section 5 concludes with key findings.

2. System modeling

2.1. MFCS powertrain configuration

This study employs a parallel architecture due to its inherent advantages in enabling independent control of each FC stack and enhancing system redundancy. In this design, a unidirectional DC-DC converter connects each FC stack to the DC bus, while the ESS is connected via a bidirectional DC-DC converter to allow for both charging and discharging. The configuration of the parallel MFCS powertrain is depicted in Fig. 1, and the number of stacks can vary based on the application.

The MFCS operates under a power balance constraint, expressed in (1), which ensures that total power demand is met by the available sources:

$$\frac{P_{Req}}{\eta_{DC-AC}} + P_{Aux} = \eta_{DC-DC,FC} \sum_{i=1}^{N_{st}} P_{FC,i} + \eta_{DC-DC,bat} P_{bat} \tag{1}$$

Here, P_{Req} is the load demand, P_{Aux} is auxiliary power of FCs, $P_{FC,i}$ is the ith FC stack output power, and P_{bat} is the battery power. Conversion efficiencies are denoted by η_{DC-AC} (inverter), $\eta_{DC-DC,FC}$ (FC converters), and $\eta_{DC-DC,bat}$ (battery converter). N_{st} is the total number of FC systems in the MFCS.

2.2. PEMFC model

The authors of [53] proposed a semi-empirical model, which has been widely utilized in subsequent studies, to characterize the performance of PEMFCs based on experimental data. In this formulation, the output voltage of an individual cell, denoted as V_C, is expressed as the sum of four components:

$$V_C = E_{Nernst} + V_{act} + V_{ohmic} + V_{con} \tag{2}$$

where E_{Nernst} represents the reversible potential of the cell, while V_{act}, V_{ohmic}, and V_{con} correspond to the voltage losses due to activation, ohmic resistance, and concentration effects, respectively. The reversible potential is computed as (3) to (7):

$$E_{Nernst} = 1.229 - 0.85 \times 10^{-3}(T_{FC} - 298.15) + 4.3085 \times 10^{-5} T_{FC}[\ln(P_{H_2}) + 0.5 \ln(P_{O_2})] \tag{3}$$

$$V_{act} = \xi_1 + \xi_2 T_{FC} + \xi_3 T_{FC}\, ln(C_{O_2}) + \xi_4 T_{FC} \ln(I_{FC}) \tag{4}$$

$$C_{O2} = \frac{P_{O2}}{5.08 \times 10^6 \exp(-498/T_{FC})} \tag{5}$$

$$V_{ohmic} = -I_{FC} R_{internal} = -I_{FC}(\zeta_1 + \zeta_2 T_{FC} + \zeta_3 I_{FC}) \tag{6}$$

$$V_{con} = Bln\left(1 - \frac{J_{FC}}{J_{max}}\right) \tag{7}$$

The detailed explanation of the utilized FC model parameters can be found in Ref. [54].

Hydrogen consumption for the FC stack is determined using the relation provided in Ref. [55], expressed as (8):

$$\dot{m}_{H_2} = 1.05 \times 10^{-8} \frac{P_{FC}}{V_C} \tag{8}$$

Where $\dot{m}_{H_2}$ indicates the hydrogen flow rate $\left(\text{kg.s}^{-1}\right)$, and P_{FC} represents the power generated by the FC stack (W).

The main operating conditions that lead to PEMFC performance loss include start-stop cycles, variable power demand, and operation under high or low load levels [55]. The amount of PEMFC degradation (expressed as the percentage of voltage drop) can be calculated by (9) [56]:

$$Deg_{FC} = \left(k_s n_s + k_f \Delta P_{FC} + k_l t_l + k_h t_h\right) \tag{9}$$

where k_s, k_f, k_l, and k_h represent the coefficients corresponding to start-stop events, fast load changes, low-power operation (defined as power below 5 % of the FC rated power), and high-power operation (defined as power exceeding 90 % of the FC rated power), respectively. The numerical values of these coefficients are provided in Table 2, based on data reported in Ref. [56]. Additionally, n_s denotes the number of start-stop events, ΔP_{FC} indicates the magnitude of load variation (W), while t_l and t_h represent the durations of low-power and high-power operations (h), respectively.

2.3. Battery model

The ESS in this study is a lithium-ion battery, which is utilized to recover energy during braking and regulate peak power needs. Because it has been widely utilized and verified in research related to EMS, the battery is represented using an internal resistance-based model [57]

Table 3
Pre-exponential coefficient (B) values based on battery c-rate.

c	0.5	2	6	10
B	31,630	21,681	12,934	15,512

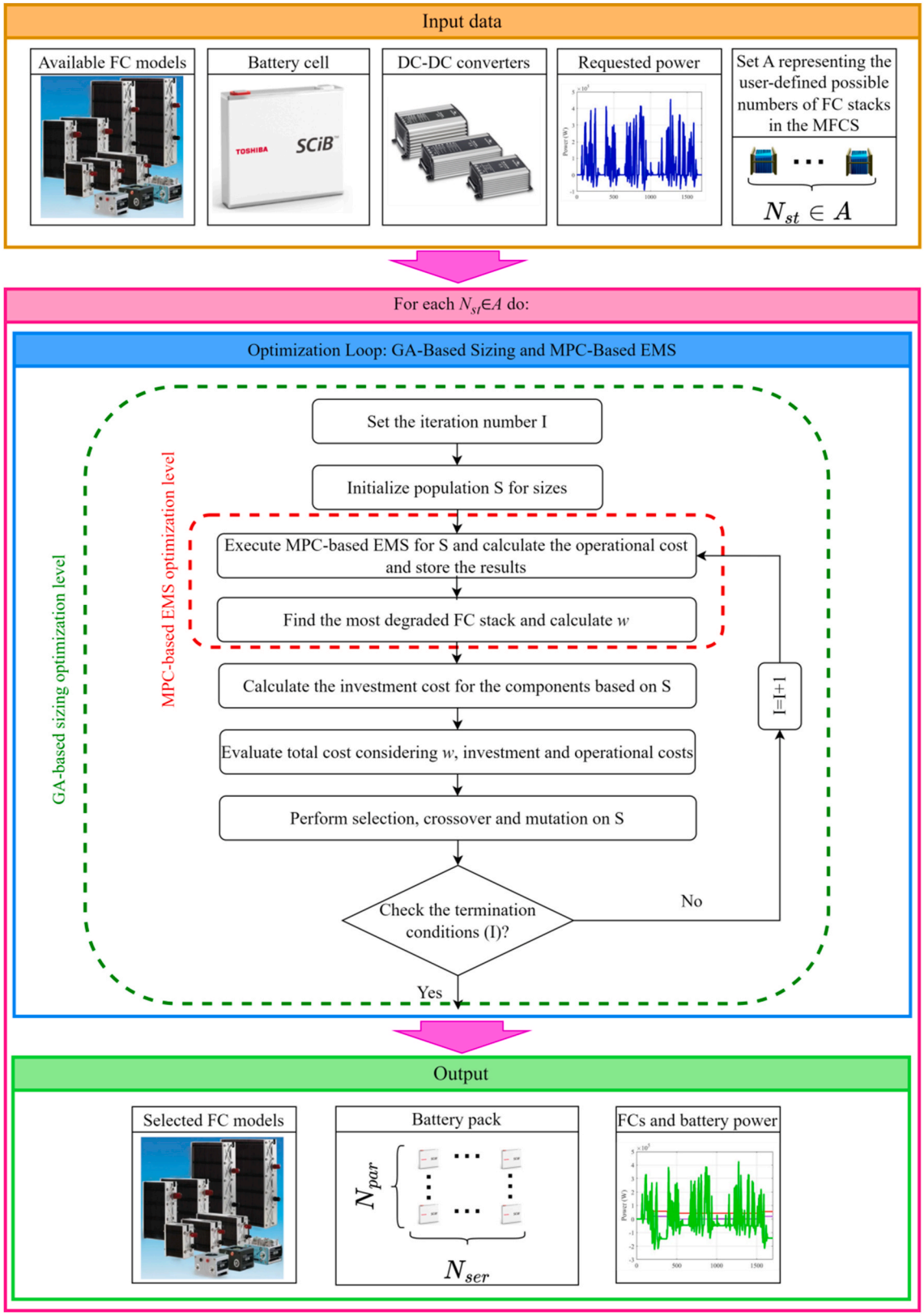

Fig. 2. GA–MPC framework for degradation-aware ISEMS in MFCSs.

During discharge, the battery current (I_{bat}) assumes a positive value, whereas it becomes negative when the battery is being charged. The battery's behavior under these operating modes is captured through equations (10)–(13) [25].

$$V_t(t) = V_{OC}(t) - I_{bat}(t)R_{bat}(t) \tag{10}$$

$$P_{bat}(t) = V_t(t)I_{bat}(t) \tag{11}$$

Table 4
GA parameters and settings in case studies 1 and 2.

Parameter	Case study 1	Case study 2
Population Size	100	50
Max. Generations	80	30
Mutation Function	Adaptive Feasible	Adaptive Feasible
Elite Count	3	3
Crossover Fraction	0.9	0.9

$$I_{bat}(t) = \frac{V_{OC}(t) - \sqrt{V_{OC}(t)^2 - 4R_{bat}(t)P_{bat}(t)}}{2R_{bat}(t)} \tag{12}$$

$$SOC(t) = SOC(t_0) - \eta_{bat}\frac{\int_{t_0}^{t} I_{bat}\, dt}{Q_{bat}} \tag{13}$$

where P_{bat}, η_{bat}, Q_{bat}, R_{bat}, V_{OC} and V_t correspond to the battery's output power (W), Coulombic efficiency, capacity (Ah), internal resistance (Ω), open-circuit voltage (V) and terminal voltage of the battery.

The continuous charge and discharge of the battery result in a gradual decline in its performance, primarily driven by irreversible physical and electrochemical transformations. A prominent indicator of battery aging is the reduction in capacity. To quantify this degradation, a control-oriented battery aging model proposed in Ref. [58] is employed in this study, whose validity has been confirmed in previous works. The model utilizes the Arrhenius-based formulation to estimate the capacity loss percentage of the battery cell (ΔQ_{cell}) with respect to its initial capacity (assumed to be 100 %) as presented in Ref. [59]:

$$\Delta Q_{cell} = B(c)\exp\left(\frac{-E_a(c)}{RT}\right)A(c)^z \tag{14}$$

where c represents the c-rate, parameter B is a pre-exponential factor that varies with the c-rate, with its values specified in Table 3. R and T refer to the universal gas constant (8.31 J.mol^{-1}.K^{-1}) and the battery cell temperature (K), respectively. The discharge throughput, A, expressed in ampere-hours (Ah), is a c-rate-dependent quantity. The exponent z, accounting for the power-law effect, is taken as 0.55. The activation energy E_a (J.mol^{-1}), which also varies with the c-rate, can be determined using (15).

$$E_a(c) = 31700 - 370.3c \tag{15}$$

As a battery reaches its end-of-life (EOL) in vehicles, it typically loses 20 % of its capacity. Accordingly, the associated discharge throughput (Ah) can be calculated using equation (16), while the total number of charge-discharge cycles at EOL is estimated by equation (17) [60].

$$A_{EOL}(c) = \left[\frac{20}{B(c)\exp\left(\frac{-E_a(c)}{RT}\right)}\right]^z \tag{16}$$

$$N_{EOL}(c) = \frac{A_{EOL}(c)}{Q_{cell}} \tag{17}$$

Consequently, the battery SOH and its rate of degradation can be formulated as follows:

$$SOH_{bat}(t) = 1 - \frac{\int_0^t |I_{bat,cell}(t)|dt}{2N_{EOL}(c)Q_{cell}} \tag{18}$$

$$\dot{SOH}_{bat}(t) = -\frac{|I_{bat,cell}(t)|}{2N_{EOL}(c)Q_{cell}} \tag{19}$$

The initial SOH is assumed to be 100 %, and $I_{bat,cell}$ represents the current of a single cell.

Table 5
Parameters heavy-duty truck.

Parameter	Symbol	Value
Vehicle mass	m	40000 (kg)
Rolling friction coefficient	c_r	0.006
Aerodynamic drag coefficient	c_d	0.73
Frontal area	A_f	9.75 (m^2)
Air density	ρ_{air}	1.225 (kg/m^3)
Gravitational acceleration	g	9.81 (m/s^2)
Differential efficiency	η_{diff}	0.97
Direct drive efficiency	η_{drive}	0.985

3. Integrated sizing and EMS design

To ensure optimal performance of FC-HEVs, an integrated optimization framework is developed to jointly address component sizing and EMS design (Fig. 2). It includes three layers: input data preparation, a GA–MPC optimization loop, and output extraction.

The input layer compiles FC models, battery specs, DC-DC converter data, requested power, and user-defined FC stack numbers (N_{st}), defining the design space and constraints. ISEMS is formulated as a mixed-integer nonlinear programming (MINLP) problem, with discrete sizing variables (e.g., FC type, battery configuration) and continuous control variables (e.g., power distribution). The objective and constraints are nonlinear due to degradation, hydrogen use, and system dynamics, making gradient-based methods unsuitable.

To solve this, a GA–MPC structure is used as a bi-level nested loop. The interaction mechanism functions as follows: The GA (outer loop) explores the discrete sizing space and generates a candidate sizing vector (S). This vector is passed to the MPC (inner loop), which uses these specific component sizes to simulate the mission profile and compute the optimal power split while respecting SOC, power limits, and degradation constraints.

After MPC execution, operational cost is calculated based on hydrogen use and component degradation. These results, specifically the operational cost and the degradation of components, are fed back to the GA. The most degraded FC stack is identified, and a weight factor (w) is computed to scale investment cost accordingly. A total cost is then formed by combining investment and operational costs using a degradation-based weighted sum (Eq. (20)). This equation serves as the mathematical coupling between the design and control layers. It penalizes low-cost but high-degradation solutions, guiding the optimization toward durable, cost-effective configurations. This total cost becomes the GA's fitness value. The GA evolves the population through selection, crossover, and mutation until a certain number of generations or convergence is obtained.

The specific parameters for the GA are calibrated to balance exploration capability with computational efficiency for two case studies of this paper (Table 4). Population size and generation limits are scaled according to the search space complexity of each case study to ensure robust convergence within a feasible timeframe.

The end result consists of optimal FC stack types, battery configuration, and the power generated by the FCs and battery, which represents a co-optimized sizing and EMS solution balancing cost and durability. This process is repeated for each $N_{st} \in A$, allowing comparison across different FC stack counts and storing the best result for each configuration.

3.1. Sizing based on GA

In the proposed framework, the sizing task is addressed using the GA, which is a population-driven metaheuristic capable of effectively handling optimization problems characterized by mixed-integer variables, nonlinearity, and non-convexity [63]. The GA determines the optimal configuration of the FC system and battery pack by evolving a population of candidate solutions over successive generations. Each

Table 6
Specifications of nine off-the-shelf FC stack models from PowerCell Group [61, 62].

	Rated power (kW)	No. of cells
V-stack	3	24
	6.5	48
	10	72
	26	192
	35.5	264
P-stack	78	275
	95	335
	119	419
	129	455

individual in the population represents a sizing candidate defined by a chromosome composed of discrete genes.

The decision variables include the types of FC stacks selected for the MFCS and the configuration of the battery pack. Specifically, the genes encode.

- The type index of each FC stack (discrete, selected from the available FC models),
- The number of battery cells in series,
- The number of battery cells in parallel.

The length of each chromosome is equal to $N_{st}+2$, where N_{st} represents the FC stacks number and the additional two entries correspond to the battery configuration (series and parallel cell counts). Each chromosome is represented as a vector S, for example $S=[3, 4, 4, 6, 205, 8]$, which denotes a configuration with four FC stacks (model indices 3, 4, 4, and 6), 205 battery cells in series, and 8 in parallel. This encoding allows the algorithm to evaluate different combinations of FC and battery configurations in a compact and flexible manner. Based on the structure of vector S, in which all elements are discrete integers, an integer version of the GA is adopted to perform the optimization.

The GA starts with an initial population generated randomly within predefined bounds. It evaluates each individual using the nested MPC-based EMS and total cost function. Based on the fitness values, individuals are selected for reproduction, and new candidates are generated through crossover and mutation. This evolutionary process is repeated across generations until a termination criterion is satisfied.

The total cost associated with each sizing candidate is computed using a weighted sum of the investment and operational costs. The investment cost reflects the capital expenses associated with the selected FC and battery configurations. However, a direct summation of the investment cost (a long-term capital expenditure) and the operational cost (a short-term expense per single mission) would result in an unbalanced objective function dominated entirely by the hardware cost. To resolve this time-scale mismatch and derive a cost function supported by the physical lifespan of the components, a degradation-based scaling factor w is introduced. To account for the mismatch in time scale between short-term operation and long-term investment, a degradation-based weight factor w is introduced. The final total cost (C_{tot}), used as the fitness metric within the GA, is formulated to represent the total cost per mission and is defined as (20):

Table 7
Battery cell parameters utilized in case study 1.

Parameter	Symbol	Value
Capacity (Ah)	Q_{cell}	10
Nominal voltage (V)	$V_{cell,nom}$	2.4
Max. power (W)	$P_{cell,max}$	1800
Min. power (A)	$P_{cell,min}$	−1500

$$C_{tot}=\frac{C_{inv}}{w}+C_{op} \tag{20}$$

where C_{inv} is the investment cost, C_{op} is the operational cost obtained from the EMS evaluation, and w is a scaling factor derived from the degradation of the most degraded FC stack. The operational cost, which reflects short-term performance and degradation during the mission, is evaluated using the EMS and is detailed in Section 3.2.

The investment cost is expressed as (21):

$$C_{inv}=\sum_{i=1}^{N_{st}} c_{FC}.P_{FC,i,max}+c_{bat}.N_{ser}.N_{par}.Q_{cell}.V_{cell,nom} + \sum_{i=1}^{N_{st}} c_{con}.P_{FC,i,max}+c_{con}.max\left(P_{bat,max},\left|P_{bat,min}\right|\right) \tag{21}$$

where $P_{FC,i,max}$ is the ith FC stack rated power. Parameters c_{FC}, c_{bat} and c_{con} are the unit costs of the FC, battery, and converter, respectively. In this study, $c_{FC}=250\ \$.kW^{-1}$, $c_{bat}=178.41\ \$.kWh^{-1}$, $c_{con}=100\ \$.kW^{-1}$ [64]. N_{ser} and N_{par} represent the number of battery cells in series and parallel. $V_{cell,nom}$ is the nominal voltage of a battery cell. $P_{bat,max}$ and $P_{bat,min}$ are the maximum and minimum powers of battery pack, respectively.

The weight w is defined as (22):

$$w=\frac{Deg_{FC,allowed}}{max_i\left(Deg_{FC,i}\right)} \tag{22}$$

where $Deg_{FC,allowed}$ is the highest allowable degradation of the FC stacks, and $Deg_{FC,i}$ is the ith FC stack degradation.

The derivation of this formula is based on the definition of component EOL. In commercial applications, the EOL of a FC stack is empirically defined as the point where performance drops by a specific percentage (typically 10 % voltage loss) from its beginning-of-life.

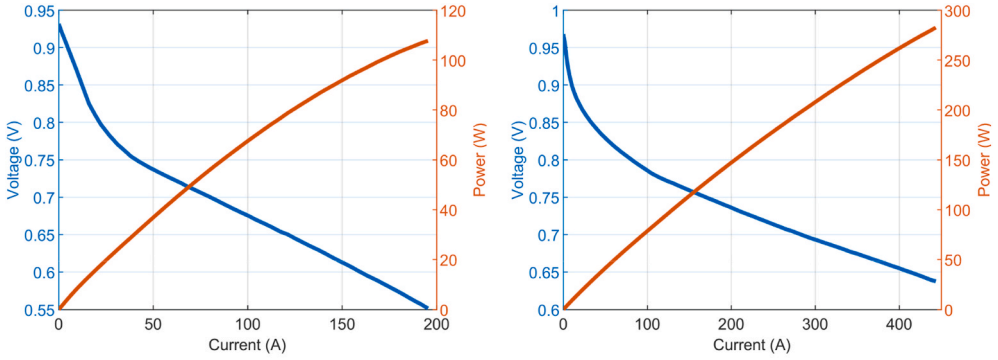

Fig. 3. Polarization and I-P curves of (a) V-stack and (b) P-stack models used in case study 1.

Table 8
Optimal configurations from ISEMS for different FC stack counts in case study 1, including costs and degradation levels.

	Optimal configuration		Costs ($)				Degradations (%)	
No. of FC stacks	FC stack sizes (kW)	Battery (N_{ser}, N_{par})	C_{inv}	C_{inv}/w	C_{op}	C_{tot}	Max. FCs	Battery
1	119	180s, 9p	339995.91	106.04	16.96	123.00	0.0031	0.0005
2	10, 95	213s, 8p	349879.43	77.14	13.58	90.72	0.0022	0.0005
3	10, 26, 78	196s, 8p	326121.55	69.88	13.41	83.29	0.0021	0.0005
4	2 × 35.5, 78, 95	156s, 9p	339003.85	74.41	19.77	94.18	0.0022	0.0006
5	4 × 35.5, 78	150s, 8p	288176.38	61.62	18.03	79.65	0.0021	0.0007
6	10, 2 × 26, 2 × 35.5, 78	141s, 8p	272192.58	63.65	17.20	80.85	0.0023	0.0007

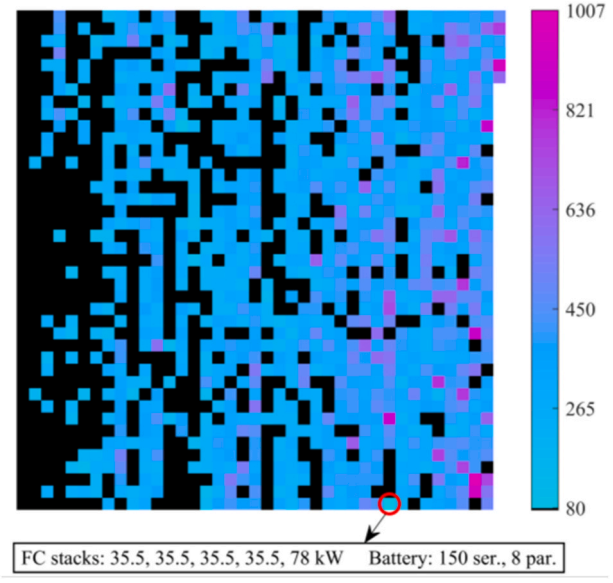

Fig. 4. Total cost heatmap of five-stack FCS configurations in case study 1.. (Each colored cell represents a unique configuration; x- and y-axes are arbitrary indices with no physical meaning.)

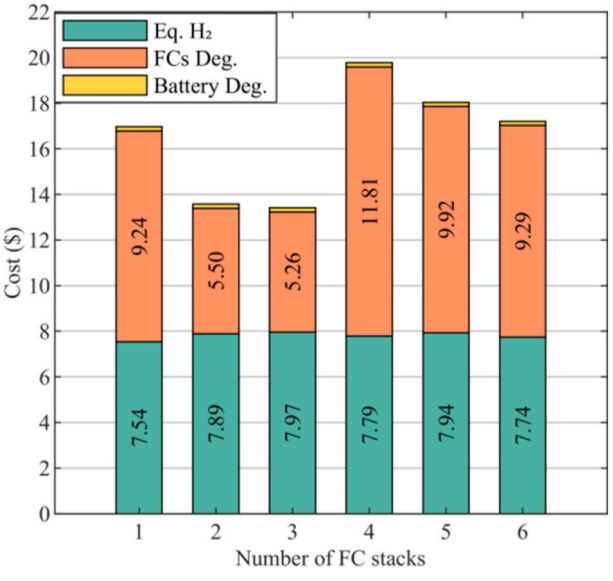

Fig. 5. Operational cost breakdown by number of FC stacks in case study 1.

Therefore, $Deg_{FC,allowed}$ represents the total "degradation budget" available to the stack. Since $Deg_{FC,i}$ represents the degradation consumed during one specific mission profile, the ratio w physically represents the projected number of missions (or cycles) the system can perform before the most critical stack fails. Consequently, the term C_{inv}/w in (20) effectively converts the total capital expenditure into an amortized investment cost per mission. This ensures that the optimization objective C_{tot} is a consistent summation of the operational cost of the mission plus the depreciation cost of the hardware attributed to that mission. This formulation penalizes designs that may be cheap to build but degrade rapidly (low w, high depreciation), guiding the algorithm toward solutions that balance initial cost with long-term durability.

The sizing problem is subject to a set of constraints, as expressed in (23) to (25), that govern the selection of FC models and battery configuration bounds.

$$S_i \in \{1, 2, \ldots, N_{FC,models}\}, \forall i = 1, \ldots, N_{st} \tag{23}$$

$$N_{ser,min} \leq N_{ser} \leq N_{ser,max} \tag{24}$$

$$N_{par,min} \leq N_{par} \leq N_{parr,max} \tag{25}$$

Where $N_{FC,models}$ is the number of available FC stack models. $N_{ser,min}$, $N_{par,min}$ are the minimum numbers of battery cells in series and parallel, and $N_{ser,max}$ and $N_{parr,max}$ are the maximum numbers of battery cells in series and parallel, respectively, based on the voltage constraints of the problem.

3.2. EMS based on MPC

This section presents the formulation of an EMS based on MPC, implemented as the inner loop of the ISEMS framework. For each sizing candidate S, the operational cost C_{op} is evaluated using an MPC strategy. MPC is used to determine the optimal power split between the FC stacks and battery over a prediction horizon, based on a receding horizon framework. At each time step, only the first control action is applied, and the optimization is repeated at the next step using updated measurements.

The system dynamics are modeled in a discrete-time state-space form as shown in (26) to (29) where the SOC is the state variable (x), the power of FC (P_{FC}) is the control variable (u) and the requested power (P_{req}) is a disturbance (d) [36].

$$\Delta x(t+1) = A\Delta x(t) + B\Delta u(t) + E\Delta d(t) \tag{26}$$

$$\Delta x(t) = \Delta SOC(t) = \frac{(SOC(t) - SOC(t-1))}{\Delta t} \tag{27}$$

$$\Delta u(t) = \Delta P_{FC}(t) = \frac{(P_{FC}(t) - P_{FC}(t-1))}{\Delta t} \tag{28}$$

$$\Delta d(t) = \Delta P_{req}(t) = \frac{(P_{req}(t) - P_{req}(t-1))}{\Delta t} \tag{29}$$

Two critical MPC design parameters, the prediction (P_h) and control (C_h) horizons, dictate the trade-off between control optimality and computational burden. In this work, both horizons are set to 10 s, a value selected based on established findings in FC-HEVs literature [36,56,65]. These studies demonstrate that a 10-s window provides sufficient

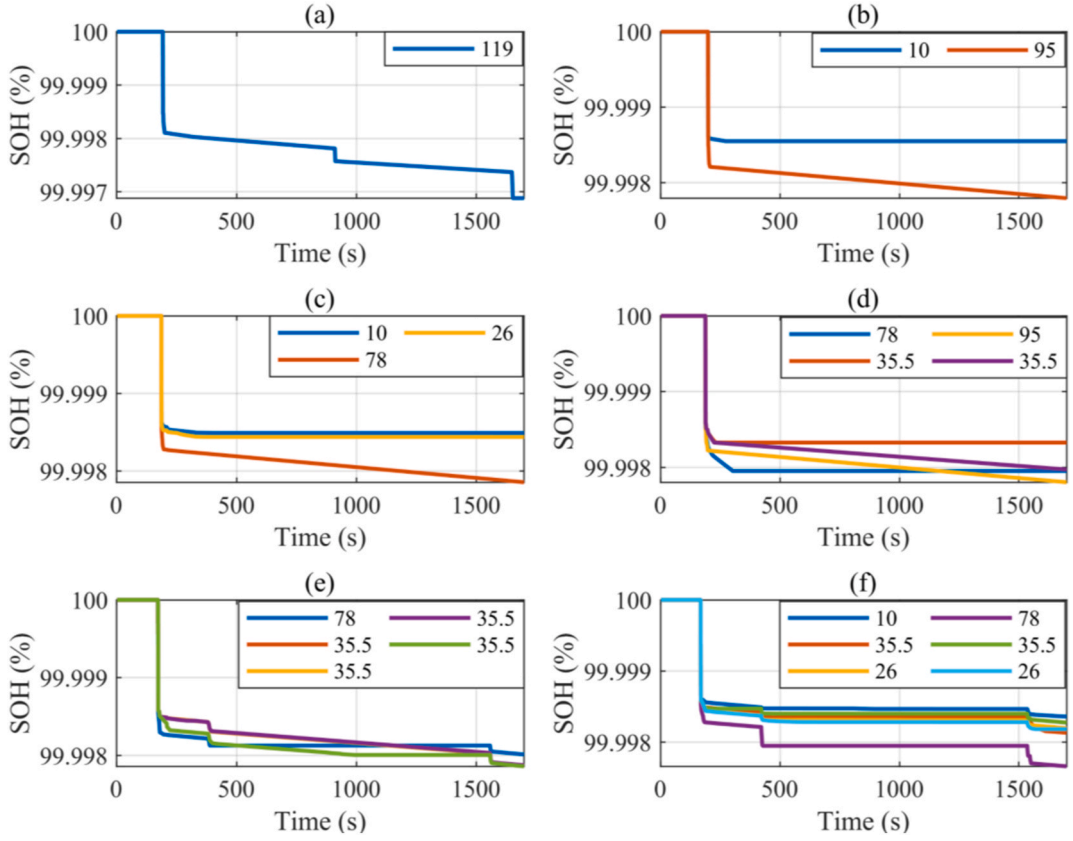

Fig. 6. SOH trajectories of FC stacks under degradation-aware EMS for (a) 1-stack, (b) 2-stack, (c) 3-stack, (d) 4-stack, (e) 5-stack, (f) 6-stack configurations in case study 1.

look-ahead capability for effective energy management while maintaining a computational cost feasible for the nested sizing optimization.

The operational cost is evaluated using (30) to (34). At each time step, the MPC computes an optimal sequence of FC stacks power adjustments over the defined prediction horizon. From this sequence, denoted as $\left[\Delta P^{*}_{FC}(t), \Delta P^{*}_{FC}(t+1), \ldots, \Delta P^{*}_{FC}(t+P_h-1)\right]$, only the first element is implemented in accordance with the receding horizon approach. The optimization is then repeated at the next time step using updated system states.

$$J_{EMS} = \sum_{t=1}^{T} \left[C_{H_2}(t) + C_{Deg,FC}(t) + C_{Deg,bat}(t)\right] \tag{30}$$

$$C_{H_2}(t) = c_{H_2} \sum_{p=0}^{P_h-1} \sum_{i=1}^{N_{st}} \dot{m}_{H_2,i}(t+p) \tag{31}$$

$$C_{Deg,FC}(t) = \sum_{p=0}^{P_h-1} \sum_{i=1}^{N_{st}} \frac{c_{FC} P_{FC,i,\max}\ Deg_{FC,i}(t+p)}{SOH_{FC,i}(t+p)} \tag{32}$$

$$SOH_{FC,i}(t) = 1 - \sum_{q=1}^{t-1} Deg_{FC,i}(q) \tag{33}$$

$$C_{Deg,bat}(t) = c_{bat}.Q_{bat}.V_{bat.nom} \sum_{p=0}^{P_h-1} \left(SOH_{bat}(t+p) - SOH_{bat}(t+p+1)\right) \tag{34}$$

The cost function of EMS (J_{EMS}) consists of the costs of hydrogen consumption (C_{H_2}), FC stacks degradation ($C_{Deg,FC}$) and battery degradation ($C_{Deg,bat}$) over the mission profile duration (T), which can be seen in (30). The hydrogen cost at time step t, is computed as shown in (31). This cost reflects the cumulative hydrogen consumption of all N_{st} FC stacks over the prediction horizon P_h, where the mass flow rate of ith stack ($\dot{m}_{H_2,i}$) is obtained by (8). The total consumption is then multiplied by the hydrogen price (c_{H_2}=0.004 \$.g^{-1}).

In (32), the FC stacks degradation cost at time step t is calculated over the prediction horizon, by summing the degradation costs of all N_{st} stacks. The price of ith stack is determined by multiplying its maximum power by the unit cost of FC. The degradation cost expression incorporates a penalty factor $\frac{1}{SOH_{FC,i}}$, which increases the cost contribution of stacks with lower SOH, thereby promoting operation strategies that preserve FC durability. The SOH of ith stack ($SOH_{FC,i}$) is obtained using (33), while the degradation of ith stack ($Deg_{FC,i}$) is evaluated according to (9).

Given that the starting and ending SOC values could differ, a fair comparison between different cases requires accounting for the net energy difference stored in the battery. To this end, after completing the EMS procedure, an additional term is incorporated to convert the SOC variation into its hydrogen-equivalent cost, as expressed in (35):

$$C_{H_2,\Delta SOC} = c_{H_2}.\ \frac{\left(SOC(t_0) - SOC(t_f)\right).Q_{bat}.V_{bat.nom}}{\eta_{bat}.\eta_{FC}.LHV_{H_2}} \tag{35}$$

where LHV_{H_2} is the lower heating value of hydrogen. Hence, the total operational cost of the FCS can be calculated as (36):

$$C_{op} = J_{EMS} + C_{H_2,\Delta SOC} \tag{36}$$

Hence, the equivalent hydrogen consumption cost consists of the hydrogen cost consumed by the FC stacks and the hydrogen cost associated with the difference between the initial and final SOC of the battery, as shown in (37):

$$C_{H_{2,eq}} = C_{H_2} + C_{H_2,\Delta SOC} \tag{37}$$

The constraints applied to the operation of the MFCS are defined by

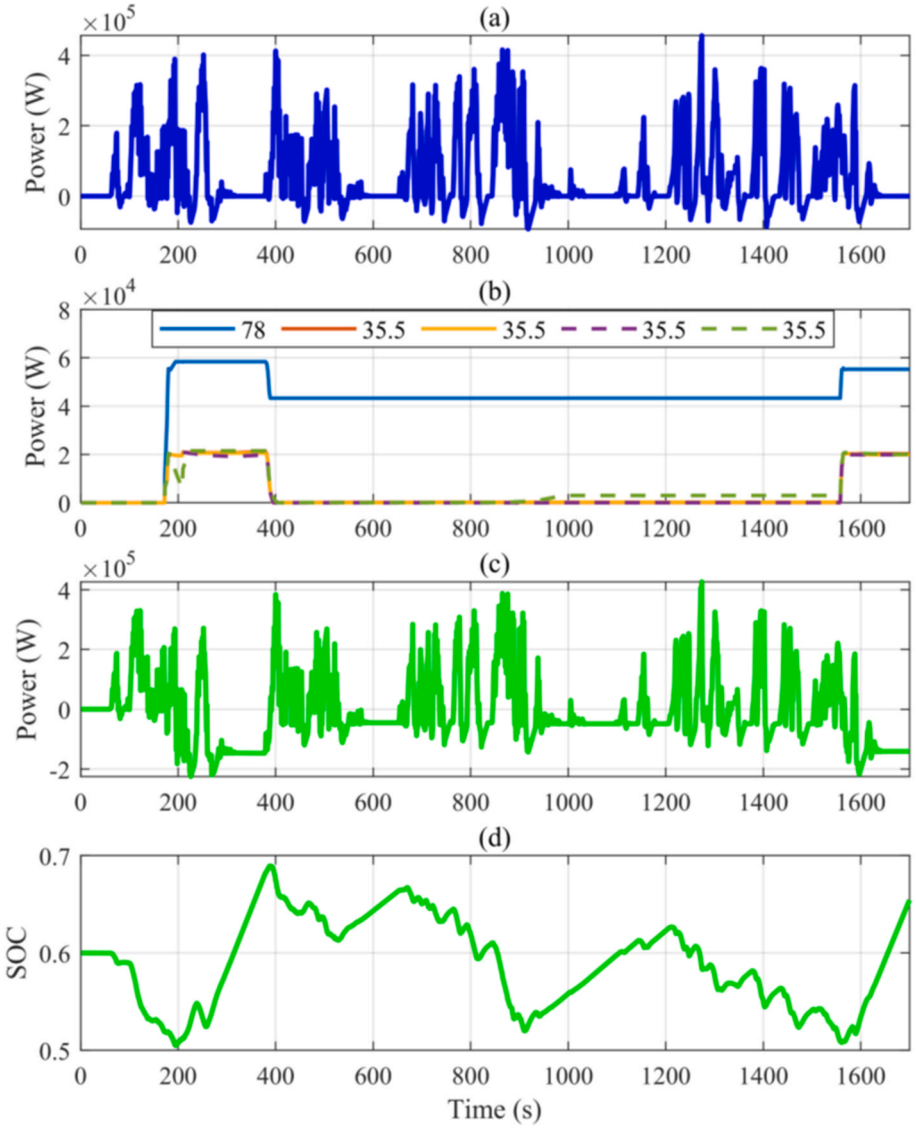

Fig. 7. The results corresponding to the five-stack configuration in case study 1: (a) requested power, (b) net output power of FC stacks, (c) battery power, and (d) battery SOC.

(25) to (30):

$$SOC_{min} \leq SOC(t+p) \leq SOC_{max} \tag{38}$$

$$P_{bat,min} \leq P_{bat}(t+p) \leq P_{bat,max} \tag{39}$$

$$P_{FC,i,min} \leq P_{FC,i}(t+p) \leq P_{FC,i,max} \tag{40}$$

$$P_{FC,i,min} \leq u_{FC,i}(t+p) \leq P_{FC,i,max} \tag{41}$$

$$\Delta P_{FC,i,min} \leq u_{FC,i}(t+p) - u_{FC,i}(t+p-1) \leq \Delta P_{FC,i,max} \tag{42}$$

where, $p \in \{1,2,\ldots,P_h\}$, and the permitted lower and higher boundaries for each state and control variable are denoted by the subscripts "min" and "max." The rate of change in the ith stack's output power is constrained by (42).

4. Results

The effectiveness of the proposed ISEMS is evaluated through simulation in this section. Two case studies are considered for validation. In the first case study, ISEMS is employed to determine the optimal configuration of FC stacks and the battery pack size for a heavy-duty truck. The resulting configuration is then compared with a benchmark configuration reported in the literature. In the second case study, the FC stacks available in the Hydrogen Research Institute of the Université du Québec à Trois-Rivières are utilized to identify the optimal system configuration. The stack characteristics, experimentally measured, are integrated into the ISEMS framework for this purpose. All simulations were performed using MATLAB R2024a on a server equipped with a 16-core 2.4 GHz processor, providing 4 GB of RAM per core.

4.1. Case study 1

4.1.1. Input data

The first case study focuses on a long-haul heavy-duty truck, where the proposed ISEMS is applied to determine the optimal sizing of the FC stacks and battery pack, as well as the power distribution between these components. Based on the vehicle specifications detailed in Table 5 [20], the power demand equations established in Ref. [66], and the speed profile of the City Suburban Heavy Vehicle Cycle & Route (CSHVR), the vehicle's power requirements are calculated.

In this case study, all nine off-the-shelf FC stack models offered by

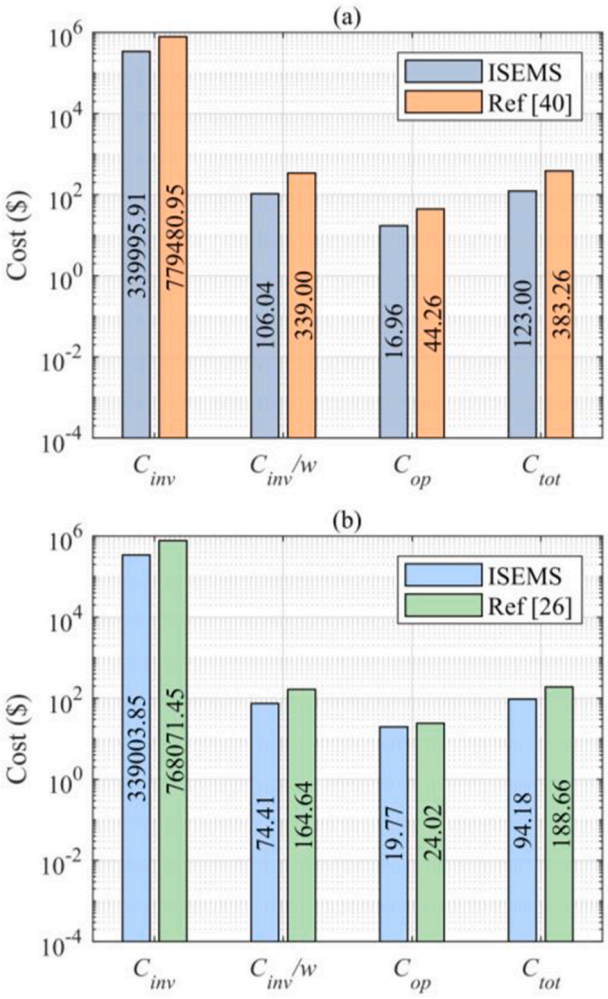

Fig. 8. Comparison of cost metrics between ISEMS and previous works: (a) single-stack ([20]), (b) four-stack ([29]).

PowerCell Group, including both P-Stack and V-Stack series, are considered. The P-Stack series features high-power, compact stacks with metallic bipolar plates and high power density, while the V-Stack series includes lower-power stacks characterized by their ease of integration, gas tolerance, and the ability to operate on both pure hydrogen and reformate gases. The specifications of these stacks are presented in Table 6, while the polarization and current-power (I-P) curves for individual cells of each model are illustrated in Fig. 3 [61,62].

The battery cell used in this case study is a high-power lithium-ion cell manufactured by Toshiba. Its specifications are presented in Table 7, and additional technical details are available in Ref. [67]. At this stage, the SOC of the battery pack is assumed to be within the range [0.5, 0.7], with an initial value of 0.6.

4.1.2. Optimal configuration

To evaluate the optimal system configuration under varying levels of FC modularity, simulations were conducted for different numbers of stacks, ranging from $N_{st} = 1$ to $N_{st} = 6$. For each configuration, the ISEMS framework identified the optimal combination of FC stack models, the corresponding number of battery cells in series and parallel, and the power distribution strategy between the battery and the FC stacks. The resulting optimal configurations are summarized in Table 8.

Considering on this table, the five-stack configuration yields the lowest total cost ($79.65), driven by the lowest normalized investment cost per mission ($61.62) and a moderate operational cost ($18.03). It comprises four 35.5 kW stacks and one 78 kW stack, with a battery of 150 series and 8 parallel cells. Both FC (0.0021 %) and battery (0.0007 %) degradation levels remain acceptable. The three-stack case also performs well, achieving the lowest operational cost ($13.41), competitive total cost ($83.29), and minimal FC degradation (0.0021 %). Although the six-stack configuration offers the lowest investment cost ($272,192.58), its total cost ($80.85) is slightly higher due to increased FC degradation (0.0023 %), which shortens system lifetime and raises the normalized investment cost. The single-stack setup shows the highest total cost ($123.00), driven by the highest normalized investment cost ($106.04) and FC degradation (0.0031 %), highlighting the drawbacks of limited modularity. Battery degradation is consistently low (0.0005–0.0007 %) across all cases, confirming effective sizing. These results confirm that higher FC modularity enhances cost-effectiveness and durability, with the five-stack design offering the most favorable trade-off for the given mission profile.

Fig. 4 presents a heatmap illustrating the total cost associated with various configurations of a five-stack FCS. Each colored cell represents a unique feasible configuration, with the color gradient ranging from cyan (lower total costs) to magenta (higher total costs). Black cells denote infeasible configurations that cannot satisfy the load constraints. The configuration with the minimum total cost, highlighted by a red circle, consists of four 35.5 kW stacks and one 78 kW stack, combined with a battery comprising 150 cells in series and 8 parallel strings. The five-stack architecture was selected for this analysis as it yields the lowest total cost compared to all other evaluated architectures with one to six stacks.

Fig. 5 illustrates the operational cost breakdown, indicating that increasing the number of FC stacks does not necessarily improve cost performance and can, in some cases, worsen degradation. The equivalent hydrogen cost remains relatively stable across all configurations ($7.54–$7.97), suggesting that hydrogen demand is primarily driven by the driving cycle and energy requirements, rather than stack count. Battery degradation costs are consistently low ($0.17–$0.19), confirming that proper battery sizing effectively mitigates aging impacts and contributes minimally to the total cost. FC degradation cost emerges as the dominant factor in operational expenses. Although modularity increases flexibility, the number of stacks must be carefully selected to avoid excessive stress on individual units. Among the evaluated setups, the three-stack configuration provides the most favorable trade-off, balancing low degradation with efficient energy supply and yielding the lowest overall operational cost.

Fig. 6 shows the SOH evolution of FC stacks for configurations with 1–6 stacks under a degradation-aware EMS. In the single-stack case, SOH declines more sharply due to the full load being carried by one unit, leading to concentrated degradation. As modularity increases, power is more evenly distributed, reducing stress on individual stacks. In configurations with three or more stacks, SOH trajectories converge despite differences in rated power, indicating that the EMS allocates power to promote uniform degradation. This highlights the EMS's role in balancing costs and durability through coordinated power distribution.

Fig. 7 illustrates results for the five-stack configuration from case study 1, selected for its lowest total cost and longest system lifetime. Subplot (a) shows highly variable requested power with several peaks. In (b), the five FC stacks collectively supply most of the power, with load distributed by a degradation-aware EMS to avoid overloading any single stack. This results in stable operation for most stacks, limiting rapid transitions and reducing degradation. Subplot (c) shows the battery responding to fast power fluctuations, supplying or absorbing energy to stabilize system output and protect FC stacks, especially evident around 400 s and 800 s. Subplot (d) confirms that battery SOC is effectively maintained within a stable range throughout the mission.

4.1.3. Validation

To validate the effectiveness of the proposed ISEMS, a comparative analysis is conducted using the configurations proposed in previous studies. Ref. [20] introduces an optimal sizing solution for a single-stack

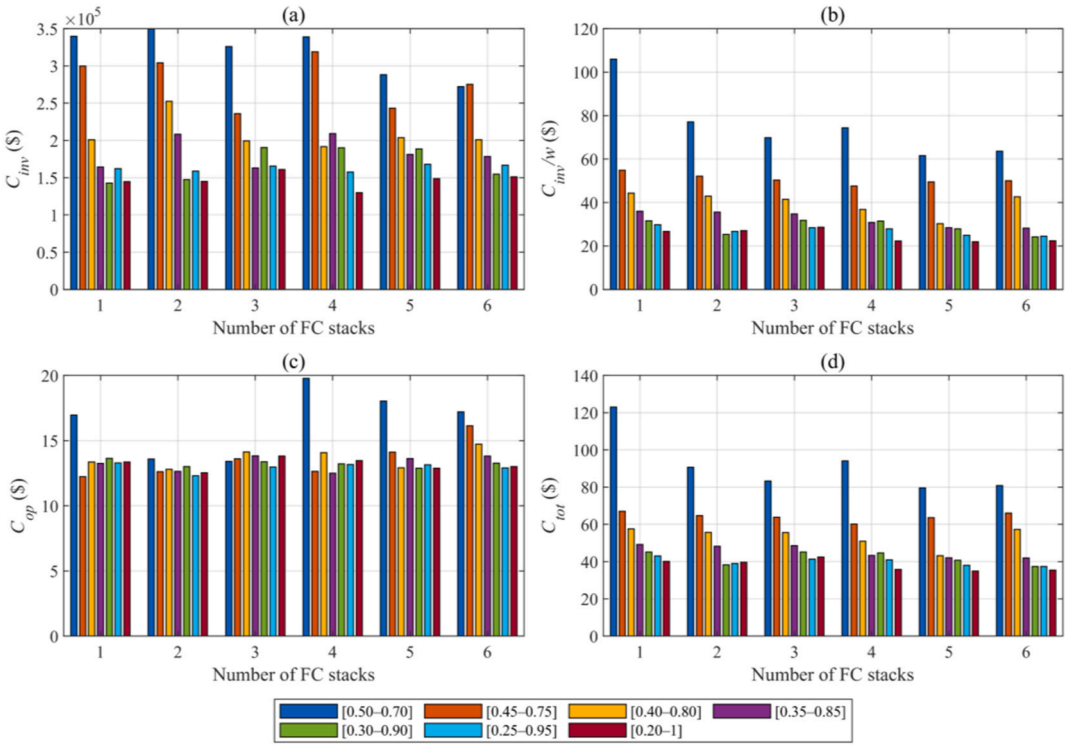

Fig. 9. Impact of SOC range on (a) investment cost, (b) investment cost per mission, (c) operational cost, and (d) total cost for different FC stack configurations in case study 1.

FCS, recommending a 334 kW FC and an 87 kWh battery. In Ref. [29], the authors adopt the sizes suggested in Ref. [20] and implement them as a four-stack configuration using FC stacks with a 75 kW power rating manufactured by PowerCell Group.

The MPC-based EMS used in this paper is applied to both the reconstructed system based on [29] and the configuration defined in Ref. [20]. The resulting performance is then compared against the proposed ISEMS under identical hardware constraints. Fig. 8 illustrates the comparative results, where subfigure (a) corresponds to the single-stack configuration of [20], and subfigure (b) presents the four-stack configuration based on [29]. All cost values are presented on a logarithmic scale to enhance visibility across several orders of magnitude.

The results clearly demonstrate the advantages of ISEMS. In both cases, C_{tot} is significantly reduced compared to the referenced strategies. Specifically, in the single-stack scenario, the proposed method results in approximately 68 % lower C_{tot} and 69 % lower C_{inv}/w compared to Ref. [20]. A deeper look at C_{inv}/w reveals that its higher value in Ref. [20] is due to two main factors. First, the absolute investment cost in Ref. [20] is substantially higher, as shown in the figure. Second, the degradation rate of the FC stack in Ref. [20] is also notably higher. In Ref. [20], the maximum degradation of the FC stack reaches 0.0043, whereas in the proposed method, it is only 0.0021. This accelerated degradation in Ref. [20] implies a shorter expected lifetime for the FC stack, meaning that the investment cost is distributed over fewer mission cycles. Consequently, the share of the investment cost per mission increases, which directly elevates C_{inv}/w.

Similar improvements are observed in the four-stack case, where all costs are lower under ISEMS. In particular, C_{tot} is reduced by nearly 50 % compared to Ref. [29], while both C_{inv} and C_{inv}/w are also notably lower. Overall, these results confirm that the proposed ISEMS can supply the required load using smaller FC stacks and battery sizes, leading to significant savings in the total system cost, including both operational cost and investment cost per mission profile. This improvement is attributed to the degradation awareness of the proposed ISEMS, implemented at both the sizing and EMS levels.

4.1.4. Sensitivity analysis

The performance of the FCS is strongly influenced by the assumptions related to the battery's SOC limits. Modifying the minimum and maximum allowable SOC changes the useable energy capacity of the battery, which directly impacts the distribution of power between the battery and FC stacks. This section evaluates the sensitivity of investment cost, operational cost, and total cost to SOC range assumptions across different FC stack configurations.

As shown in Fig. 9a, increasing the SOC window from [0.50–0.70] to [0.20–1.00] results in a consistent reduction in the investment cost across all FC stack configurations. For instance, C_{inv} in the 1-stack system decreases from 339,995.91 $ to 144,657.16 $ (−57.5 %). Similarly, the 2-stack configuration shows a reduction from 349,879.43 $ to 145,021.22 $ (−58.6 %), while the 3-stack system drops from 326,121.55 $ to 160,914.97 $ (−50.7 %). For the 4-stack, 5-stack, and 6-stack systems, the reductions are from 339,003.85 $ to 130,051.30 $ (−61.6 %), from 288,176.38 $ to 148,689.24 $ (−48.4 %), and from 272,192.58 $ to 151,252.94 $ (−44.4 %), respectively.

The investment cost per mission profile follows the same trend, as shown in Fig. 9b. For the narrowest SOC window [0.50–0.70], C_{inv}/w is highest across all configurations, particularly in the 1-stack case (106.04 $), while the corresponding value under the [0.20–1.00] window drops from 106.04 $ to 26.75 $ (−74.8 %). Significant declines are also observed in other configurations: from 77.14 $ to 27.10 $ in the 2-stack (−64.9 %), from 69.88 $ to 28.64 $ in the 3-stack (−59.0 %), and from 74.41 $ to 22.33 $ in the 4-stack (−70.0 %). The 5-stack and 6-stack systems also show reductions from 61.62 $ to 22.04 $ and from 63.65 $ to 22.41 $, respectively.

As shown in Fig. 9c, the operational cost remains relatively stable across SOC ranges in all configurations. The variations are mostly within a narrow band of ±1 $, confirming that the expansion of the SOC window does not impair the operational cost. A minor increase is seen in some cases, such as the 3-stack configuration, where C_{op} slightly rises

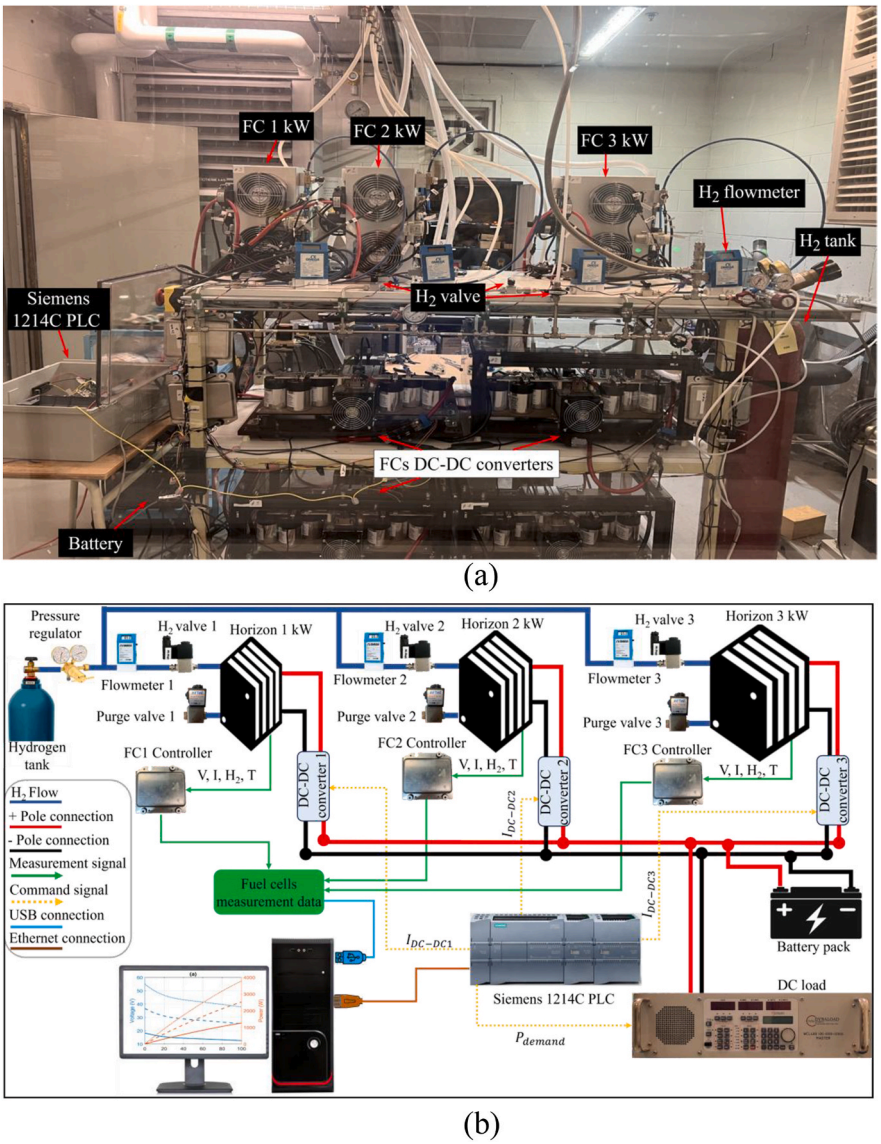

Fig. 10. Multi-stack test bench: a) real experimental setup; b) schematic diagram.

Table 9
Specifications of FC stack models from Horizon used in case study 2.

Rated power (kW)	No. of cells	Price ($)	Associated Converter Price ($)
1	24	4107.16	1964.59
2	48	5845.58	2796.06
3	72	7655.73	3662.00

from 13.41 $ to 13.81 $, while in others, like the 2-stack case, it decreases from 13.58 $ to 12.53 $. No significant operational deterioration is observed.

The total cost, depicted in Fig. 9d, captures the combined effects of investment and operational costs. Broadening the SOC range from [0.50–0.70] to [0.20–1.00] results in substantial reductions across all configurations. In the 1-stack system, C_{tot} drops from 123.00 $ to 40.11 $ (−67.4 %). For the 2-stack, 3-stack, and 4-stack cases, reductions are from 90.72 $ to 39.63 $ (−56.3 %), 83.29 $ to 42.45 $ (−49.0 %), and 94.18 $ to 35.80 $ (−62.0 %), respectively. The 5-stack and 6-stack configurations decrease from 79.65 $ to 34.92 $ and from 80.85 $ to 35.41 $, both showing cost reductions of over 55 %.

These results demonstrate that wider SOC ranges enable greater exploitation of the battery's energy capacity, allowing the powertrain to rely less on the FC system and consequently reduce its size and cost. The improvement in cost-effectiveness is most prominent when moving from [0.50–0.70] to [0.20–1.00], but the downward trend is also apparent across intermediate SOC ranges. These findings reinforce the importance of careful SOC range selection in hybrid FC-battery design, as it directly impacts sizing decisions and overall economic performance.

4.2. Case study 2

4.2.1. Input data

The second case study is based on the experimental setup available at the Hydrogen Research Institute of the Université du Québec à Trois-Rivières, using the multi-stack test bench shown in Fig. 10. In this study, the test bench is used to extract performance data from Horizon FC stacks as part of case study 2. The hybrid setup consists of three closed-cathode Horizon PEMFC stacks rated at 1 kW, 2 kW, and 3 kW, connected in a parallel architecture with a lithium-ion battery pack. Each FC stack is connected to a DC-DC converter that boosts the FC output voltage to match the battery pack voltage, which serves as the DC bus. Each FC stack is also monitored by an individual FC controller that collects real-time data, including voltage, current, hydrogen flow rate,

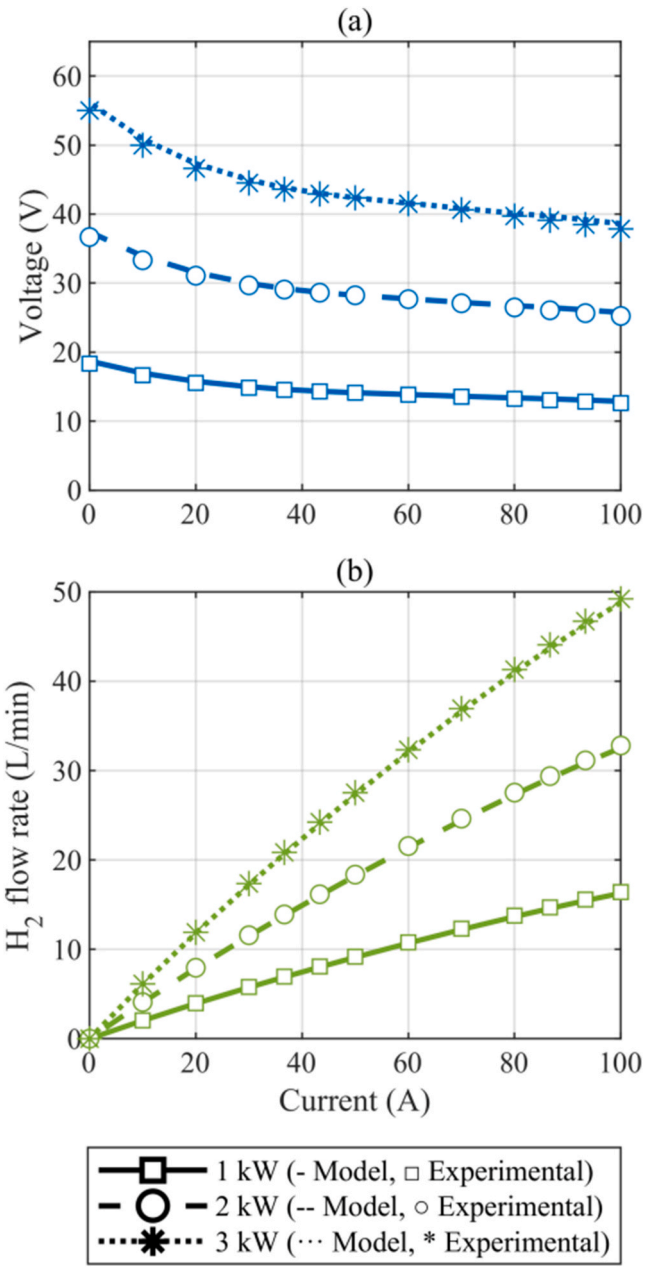

Fig. 11. Modeled and experimental (a) polarization curve, and (b) hydrogen flow rate for Horizon FC stacks used in case study 2.

Table 10
Battery cell parameters utilized in case study 2.

Parameter	Symbol	Value
Capacity (*Ah*)	Q_{cell}	2.9
Nominal voltage (*V*)	$V_{cell,nom}$	2.4
Max. power (*W*)	$P_{cell,max}$	520
Min. power (*A*)	$P_{cell,min}$	−410

and temperature. A DC electronic load is used to emulate various power demands. A Siemens 1214C PLC sends the power demand to the DC load and provides the reference current signals to the DC-DC converters by adjusting their PWM control. Measurement and control signals are exchanged between the controllers, converters, and PLC, with real-time data acquisition handled via USB and Ethernet connections.

In this case, the proposed ISEMS is employed to determine the optimal sizing of the FC stacks and battery pack, as well as the power distribution between these components. The characterization data for the FC stacks, including polarization curves and hydrogen flow measurements, are experimentally obtained from the available test bench and subsequently integrated into the ISEMS framework. The power demand profile is obtained using the Worldwide harmonized Light-duty vehicles Test Cycle (WLTC) Class 3 driving cycle, which is suitable for evaluating powertrain performance under a wide range of operating conditions.

In this case study, three commercial FC stack models manufactured by Horizon are considered. These stacks, with rated powers of 1, 2, and 3 kW, are available in the laboratory test bench and have been experimentally characterized. Their specifications are listed in Table 9. Fig. 11 compares the modeled and experimental performance of the FC stacks at 1 kW, 2 kW, and 3 kW. In Fig. 11a, the polarization curves show the expected voltage drop with increasing load, while a close alignment between the model (solid, dashed, and dotted lines) and the experimental points (square, circle, and star) is observed. The experimental voltages are slightly lower than the modeled values, with a maximum deviation of approximately 3 % across all operating points. Fig. 11b presents the corresponding hydrogen flow rates, which increase with current as predicted by the model. The experimental measurements follow the same trend, showing only minor deviations, and the hydrogen consumption is slightly higher than the modeled predictions, with a maximum difference of about 1 %.

In this case study, a high-power lithium-ion cell produced by Toshiba is selected as the battery technology. The key parameters characterizing this cell are summarized in Table 10, with more detailed technical information available in Ref. [67]. The battery pack operates within a predefined SOC window of [0.5, 0.7], and the initial SOC is set to 0.6.

High-power PEMFC stacks suitable for heavy-duty applications are generally not available for laboratory testing due to their high cost. However, the fundamental electrochemical behavior of PEMFCs is scale-independent, and the polarization and efficiency curves of high-power stacks follow the same form as those of low-power stacks, with the main difference being the number of cells connected in series. Therefore, the experimental 1–3 kW stacks effectively capture the stack-level dynamics required for model validation. Moreover, since the primary complexity of HDVs arises from their multi-stack architecture, validating the proposed ISEMS on a multi-stack configuration at laboratory scale ensures direct scalability to HDV-scale systems.

4.2.2. Optimal configuration

To evaluate the impact of FC modularity, configurations with 1–5 stacks were simulated using the ISEMS framework, which optimized stack selection, battery sizing, and power sharing. As shown in Table 11, the single-stack configuration was infeasible under the given mission, unable to meet power demand. Among feasible options, the two-stack setup achieved the lowest total cost ($3.55), driven by a minimal normalized investment cost ($2.95) and low operational cost ($0.60). It employed two 2 kW stacks and a 25s–10p battery, with low FC (0.0017 %) and battery (0.0003 %) degradation. The three- and four-stack configurations showed nearly identical degradation values and retained the same battery size but incurred higher total costs of $4.14 and $4.72, respectively, due to increased modularity and investment cost, without notable gains in durability. The five-stack setup significantly raised total cost ($10.80), mainly due to higher investment cost ($33,208.04) and increased FC degradation (0.0030 %), which reduced system life and elevated the normalized investment per mission ($9.84). Battery degradation remained minimal (0.0003–0.0004 %) across all feasible configurations, indicating adequate battery sizing and limited electrochemical stress. Overall, moderate modularity, particularly the two- or three-stack configurations, provided the most cost-effective and durable solution for the evaluated mission profile.

Fig. 12 illustrates the SOH evolution of FC stacks for 2- to 5-stack configurations in case study 2 under the degradation-aware EMS. Each

Table 11
Optimal configurations from ISEMS for different FC stack counts in case study 2, including costs and degradation levels.

	Optimal configuration		Costs ($)				Degradations (%)	
No. of FC stacks	FC stack sizes (kW)	Battery (N_{ser}, N_{par})	C_{inv}	C_{inv}/w	C_{op}	C_{tot}	Max. FCs	Battery
1	–	–	–	–	–	–	–	–
2	2 × 2	25, 10	17593.71	2.95	0.60	3.55	0.0017	0.0003
3	2 × 1, 2	25, 10	21095.58	3.54	0.61	4.14	0.0017	0.0003
4	4 × 1	25, 10	24597.44	4.11	0.61	4.72	0.0017	0.0003
5	4 × 1, 2	25, 9	33208.04	9.84	0.95	10.80	0.0030	0.0004

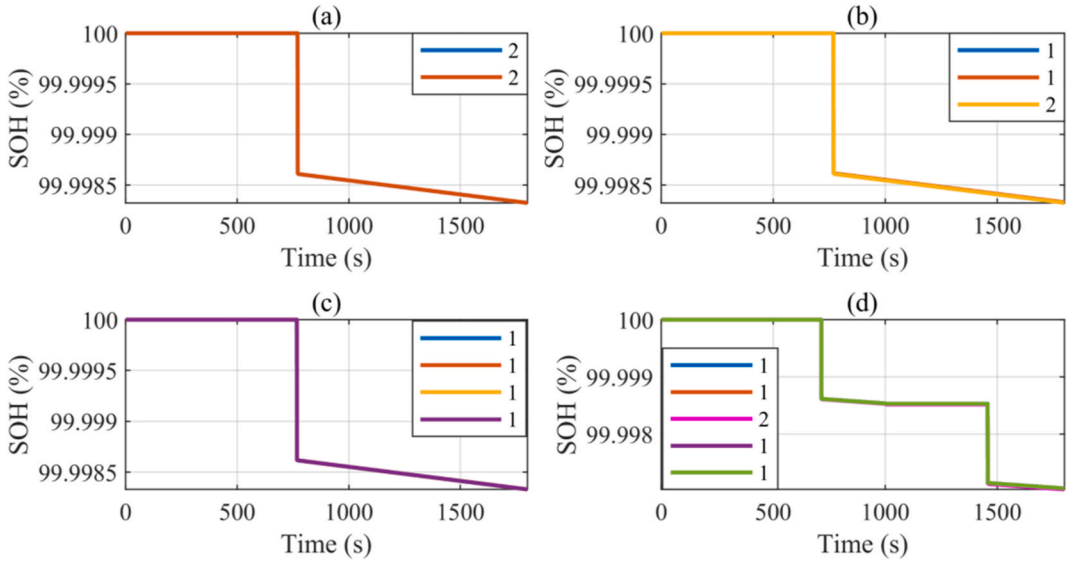

Fig. 12. SOH trajectories of FC stacks under degradation-aware EMS for (a) 2-stack, (b) 3-stack, (c) 4-stack, (d) 5-stack configurations in case study 2.

subplot represents a modularity level, with legends indicating stacks rated powers in kW. Across all configurations, SOH trajectories remain nearly identical, demonstrating the EMS's ability to balance power distribution, even with heterogeneous stacks.

In the 2-stack configuration (Fig. 12a), a sharp SOH drop appears around 800 s due to the activation of the 2 kW stacks, after which both units exhibit overlapping degradation profiles. The 3-stack setup (Fig. 12b) follows a similar trend, as all SOH trajectories remain closely aligned despite differences in rated power. In the 4-stack configuration (Fig. 12c), the SOH curves fully overlap throughout the mission. In the 5-stack configuration (Fig. 12d), all SOH trajectories exhibit two distinct degradation steps. These steps correspond to switching phases where stacks are activated dynamically based on system demand. Despite these transitions, the SOH curves remain closely grouped.

Overall, the results confirm that the degradation-aware EMS applies a consistent load balancing strategy that harmonizes stack degradation across different modular configurations. This uniformity in SOH evolution supports effective utilization of available resources and contributes to the long-term durability of the FC system.

Fig. 13 presents results for the dual-stack FC configuration from case study 2, selected due to its lowest total cost among all configurations. Fig. 13a depicts a highly dynamic requested power profile with several sharp peaks, particularly in the latter part of the mission. Fig. 13b shows the output power of the two 2 kW FC stacks, which remain off until approximately 770 s, after which they are simultaneously activated and operate continuously at their rated power. The complete overlap of the curves confirms perfectly balanced load sharing. Fig. 13c demonstrates that the battery alone supplies power before FC activation and continues to manage rapid transients by absorbing or delivering power as needed. In Fig. 13d, the SOC decreases steadily while the FCs are off, followed by a sharp recovery and gradual increase once the FCs are engaged, indicating sustained charging. Overall, the EMS ensures coordinated and continuous FC operation after activation, with the battery supporting transient conditions and maintaining SOC stability throughout the mission.

4.3. Robustness against parameter variations

The proposed ISEMS framework relies on the profile of the FC polarization and efficiency curves rather than static operating points. In a real-world operational environment, parameters such as temperature, air stoichiometry, pressure, and humidity represent nominal operating conditions that are actively regulated by the balance of plant to maintain the stack within the manufacturer's specified performance window. While minor real-world fluctuations in these variables may cause slight deviations in instantaneous efficiency and polarization curve, they do not alter the fundamental characteristic shape of the curves used by the optimization algorithm. Consequently, the optimization logic remains valid and robust against these minor transient disturbances. Furthermore, regarding aging variability, previous studies on online parameter identification using Kalman Filters such as [68,69] have demonstrated that physical degradation manifests primarily as a parametric shift in the polarization curve—specifically, an increase in internal resistance or a drop in open-circuit voltage—rather than a fundamental structural change in the system's behavior. Crucially, in the MPC simulation, this degradation effect is explicitly considered, and the polarization curve is dynamically updated based on the accumulated degradation amount. The proposed ISEMS anticipates these shifts by incorporating EOL conditions directly into the sizing constraints. By optimizing for the worst-case degradation scenario via the weighting factor (w), the resulting system architecture is inherently robust against aging rate variability and parametric uncertainties encountered during long-term

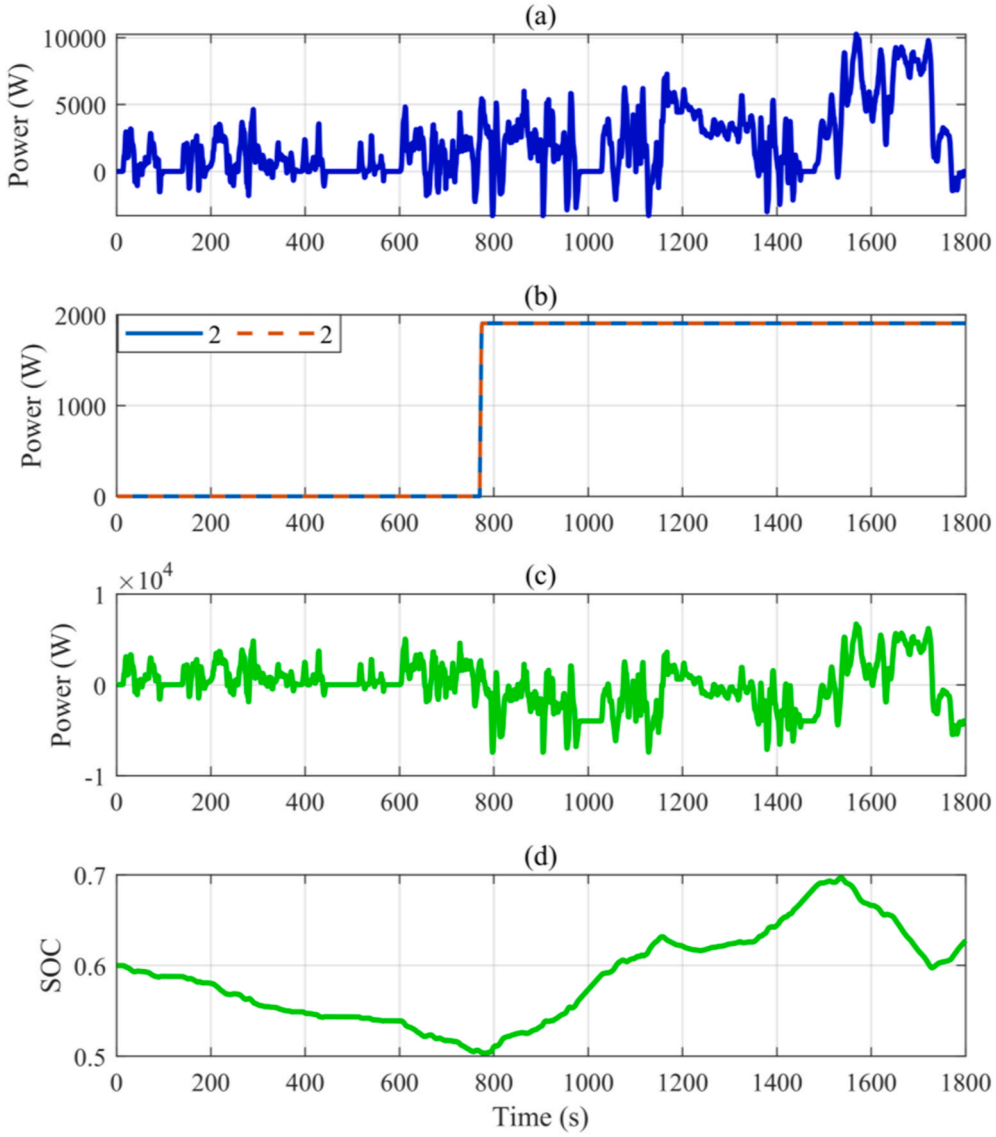

Fig. 13. The results corresponding to the dual-stack configuration in case study 2: (a) requested power, (b) net output power of FC stacks, (c) battery power, and (d) battery SOC.

operation.

5. Conclusion

This paper proposed a degradation-aware ISEMS for MFCSs in HDVs. By embedding degradation models directly into a hybrid GA-MPC framework, the method simultaneously optimized component sizing and power distribution. The key findings are summarized as follows:

Cost and Durability Improvement: In the long-haul truck case study, the proposed approach reduced the total cost by 68 % compared to single-stack and by 50 % compared to quad-stack configurations from the literature. The optimal five-stack configuration achieved the lowest total cost ($79.65) and extended system lifetime to 2209 h, significantly outperforming the 1514 h of the single-stack baseline.

Experimental Validation: Tests using real-world stack data confirmed the method's adaptability. A dual-stack configuration (2 × 2 kW) was identified as the most cost-effective solution ($3.55), offering a projected lifetime of 2984 h, whereas increasing modularity beyond this point (e.g., five stacks) reduced lifetime due to higher degradation.

Impact of Battery Utilization: Sensitivity analysis demonstrated that widening the battery SOC window (from [0.50–0.70] to [0.20–1.00]) yielded additional cost reductions of up to 67.4 %, highlighting the critical role of battery sizing in reducing FC stress.

Overall, the proposed method provides a scalable and durable solution for cost-effective MFCS design and control in HDVs. Future work will consider uncertainty in the requested power profile, investigate system performance under different hybridization factors, and determine optimal component sizes under varying FC and battery price scenarios.

CRediT authorship contribution statement

Hamid Bakhshi Yamchi: Writing – original draft, Software, Methodology, Investigation, Data curation, Conceptualization. **Mohammadreza Moghadari:** Software, Methodology, Conceptualization. **Mohsen Kandidayeni:** Writing – review & editing, Supervision, Methodology, Conceptualization. **Sousso Kelouwani:** Writing – review & editing, Supervision, Funding acquisition. **Loïc Boulon:** Writing – review & editing, Supervision, Funding acquisition.

Declaration of competing interest

The authors declare that they have no known competing financial interests or personal relationships that could have appeared to influence the work reported in this paper.

Acknowledgments

The authors would like to thank the Natural Sciences and Engineering Research Council of Canada (NSERC, Application ID: RGPIN-2025-05444), MITACS, CRIAQ (Consortium de recherche et d'innovation en aérospatiale au Québec), Flying Whales, Pratt & Whitney Canada, and MTLS-AeroStructure.

Data availability

The data that has been used is confidential.

References

[1] Tzeiranaki ST, et al. The impact of energy efficiency and decarbonisation policies on the European road transport sector. Transport Res Pol Pract 2023;170:103623.
[2] Chan CC. The state of the art of electric, hybrid, and fuel cell vehicles. Proc IEEE 2007;95(4):704–18.
[3] Rudolf T, Schürmann T, Schwab S, Hohmann S. Toward holistic energy management strategies for fuel cell hybrid electric vehicles in heavy-duty applications. Proc IEEE 2021;109(6):1094–114.
[4] Alaswad A, Baroutaji A, Achour H, Carton J, Al Makky A, Olabi A-G. Developments in fuel cell technologies in the transport sector. Int J Hydrogen Energy 2016;41(37):16499–508.
[5] Çabukoglu E, Georges G, Küng L, Pareschi G, Boulouchos K. Fuel cell electric vehicles: an option to decarbonize heavy-duty transport? Results from a Swiss case-study. Transport Res Transport Environ 2019;70:35–48.
[6] Wang Z, Zhang S, Luo W, Xu S. Deep reinforcement learning with deep-Q-network based energy management for fuel cell hybrid electric truck. Energy 2024/10/15/2024;306:132531. https://doi.org/10.1016/j.energy.2024.132531.
[7] Yamchi HB, Shahsavari H, Kalantari NT, Safari A, Farrokhifar M. A cost-efficient application of different battery energy storage technologies in microgrids considering load uncertainty. J Energy Storage 2019;22:17–26.
[8] Sulaiman N, Hannan M, Mohamed A, Majlan E, Daud WW. A review on energy management system for fuel cell hybrid electric vehicle: issues and challenges. Renew Sustain Energy Rev 2015;52:802–14.
[9] Cullen DA, et al. New roads and challenges for fuel cells in heavy-duty transportation. Nat Energy 2021;6(5):462–74. https://doi.org/10.1038/s41560-021-00775-z.
[10] Moslehi A, Kandidayeni M, Hébert M, Kelouwani S. Investigating the impact of a fuel cell system air supply control on the performance of an energy management strategy. Energy Convers Manag 2025;325:119374.
[11] Jia C, He H, Zhou J, Li J, Wei Z, Li K. Learning-based model predictive energy management for fuel cell hybrid electric bus with health-aware control. Appl Energy 2024;355. https://doi.org/10.1016/j.apenergy.2023.122228.
[12] Piras M, De Bellis V, Malfi E, Novella R, Lopez-Juarez M. Hydrogen consumption and durability assessment of fuel cell vehicles in realistic driving. Appl Energy 2024;358. https://doi.org/10.1016/j.apenergy.2023.122559.
[13] Zhang L, Liu J, Qi W, Chen Q, Long R, Quan S. A parallel modular computing approach to real-time simulation of multiple fuel cells hybrid power system. Int J Energy Res 2019;43(10):5266–83.
[14] Abdeldjalil D, Negrou B, Youssef T, Samy MM. Incorporating the best sizing and a new energy management approach into the fuel cell hybrid electric vehicle design. Energy Environ 2023. https://doi.org/10.1177/0958305x231177743.
[15] Feroldi D, Carignano M. Sizing for fuel cell/supercapacitor hybrid vehicles based on stochastic driving cycles. Appl Energy 2016;183:645–58. https://doi.org/10.1016/j.apenergy.2016.09.008.
[16] Cha M, Enshaei H, Nguyen H, Jayasinghe SG. Optimal sizing and evaluation of efficient fuel cell utilization for fuel cell battery hybrid electric ferry. Energy Convers Manag 2024;315. https://doi.org/10.1016/j.enconman.2024.118723.
[17] Venkata KoteswaraRao K, Naga Srinivasulu G, Ramesh Rahul J, Velisala V. Optimal component sizing and performance of fuel cell – battery powered vehicle over world harmonized and new European driving cycles. Energy Convers Manag 2024;300. https://doi.org/10.1016/j.enconman.2023.117992.
[18] Wang Y, Moura SJ, Advani SG, Prasad AK. Optimization of powerplant component size on board a fuel cell/battery hybrid bus for fuel economy and system durability. Int J Hydrogen Energy 2019;44(33):18283–92. https://doi.org/10.1016/j.ijhydene.2019.05.160.
[19] Knibbe R, et al. Optimal battery and hydrogen fuel cell sizing in heavy-haul locomotives. J Energy Storage 2023;71. https://doi.org/10.1016/j.est.2023.108090.
[20] Anselma PG, Belingardi G. Fuel cell electrified propulsion systems for long-haul heavy-duty trucks: present and future cost-oriented sizing. Appl Energy 2022;321:119354.
[21] Nie Z, Feng Y, Lian Y. Deep reinforcement learning-based hierarchical control strategy for energy management of intelligent fuel cell hybrid electric vehicles. Energy 2025:136281.
[22] Wang T, Li Q, Yin L, Chen W. Hydrogen consumption minimization method based on the online identification for multi-stack PEMFCs system. Int J Hydrogen Energy 2019;44(11):5074–81.
[23] Guo X, An G. A hierarchical optimization energy management strategy based on AECMS-MPC for heavy-duty fuel cell hybrid vehicles. Energy 2025:137591.
[24] Song D, Wu Q, Huang Y, Zeng X, Yang D. Energy-thermal collaborative management considering powertrain thermal characteristics for fuel cell vehicles in low-temperature environment. Energy 2025;320:135102.
[25] Zhou H, Yu Z, Wu X, Fan Z, Yin X, Zhou L. Dynamic programming improved online fuzzy power distribution in a demonstration fuel cell hybrid bus. Energy 2023;284:128549.
[26] Tao S, et al. Energy management strategy based on dynamic programming with durability extension for fuel cell hybrid tramway. Railway Engineering Science 2021;29(3):299–313. https://doi.org/10.1007/s40534-021-00247-w.
[27] Meng X, Li Q, Zhang G, Chen W. Efficient multidimensional dynamic programming-based energy management strategy for global composite operating cost minimization for fuel cell trams. IEEE Transactions on Transportation Electrification 2021;8(2):1807–18.
[28] Ghaderi R, Kandidayeni M, Boulon L, Trovão JP. Q-learning based energy management strategy for a hybrid multi-stack fuel cell system considering degradation. Energy Convers Manag 2023;293:117524.
[29] Yamchi HB, Kandidayeni M, Kelouwani S, Boulon L. Constrained exploration method for optimal energy management in hybrid multi-stack fuel cell vehicles. Energy Convers Manag 2024;316:118841.
[30] Kandidayeni M, Yamchi HB, Trovao JPF. Advancing hydrogen and fuel cell technologies for sustainable aviation: challenges and future directions. In: Paolini V, Petracchini F, editors. Hydrogen and low-carbon fuels in circular bio-economy: assessment methodologies, production technologies and sector-specific applications. Cham: Springer Nature Switzerland; 2025. p. 255–304.
[31] Peng F, Xie X, Wu K, Zhao Y, Ren L. Online hierarchical energy management strategy for fuel cell based heavy-duty hybrid power systems aiming at collaborative performance enhancement. Energy Convers Manag 2023;276:116501.
[32] Wang T, Li Q, Yin L, Chen W, Breaz E, Gao F. Hierarchical power allocation method based on online extremum seeking algorithm for Dual-PEMFC/Battery hybrid locomotive. IEEE Trans Veh Technol 2021;70(6):5679–92. https://doi.org/10.1109/tvt.2021.3078752.
[33] Chai X, Ma R, Song J, Sun H, Wang C, Feng Z. An energy management strategy for all electric aircraft based on multi-stack fuel cells. In: 2023 IEEE transportation electrification conference & Expo (ITEC). IEEE; 2023. p. 1–6.
[34] Li Q, et al. Online extremum seeking-based optimized energy management strategy for hybrid electric tram considering fuel cell degradation. Appl Energy 2021;285:116505.
[35] Soltani AK, Boulon L, Hu X. Fully decentralized energy management strategy based on model predictive control in a modular fuel cell vehicle. In: 2021 IEEE transportation electrification conference & Expo (ITEC). IEEE; 2021. p. 767–70.
[36] Moghadari M, Kandidayeni M, Boulon L, Chaoui H. Predictive health-conscious energy management strategy of a hybrid multi-stack fuel cell vehicle. IEEE Trans Vehicular Technol 2025;74(4):5542–57. https://doi.org/10.1109/TVT.2024.3512204.
[37] Jia C, Liu W, He H, Chau K. Deep reinforcement learning-based energy management strategy for fuel cell buses integrating future road information and cabin comfort control. Energy Convers Manag 2024;321:119032.
[38] Jia C, Liu W, He H, Chau K. Health-conscious energy management for fuel cell vehicles: an integrated thermal management strategy for cabin and energy source systems. Energy 2025;333:137330.
[39] Chen H, Zhang Z, Guan C, Gao H. Optimization of sizing and frequency control in battery/supercapacitor hybrid energy storage system for fuel cell ship. Energy 2020;197:117285.
[40] Madadi MH, Chitsaz I. Improving fuel efficiency and durability in fuel cell vehicles through component sizing and power distribution management. Int J Hydrogen Energy 2024;71:661–73. https://doi.org/10.1016/j.ijhydene.2024.05.276.
[41] Sadek H, Chedid R, Fares D. Power sources sizing for a fuel cell hybrid vehicle. Energy Storage 2020;2(2). https://doi.org/10.1002/est2.124.
[42] Fletcher T, Ebrahimi K. The effect of fuel cell and battery size on efficiency and cell lifetime for an L7e fuel cell hybrid vehicle. Energies 2020;13(22). https://doi.org/10.3390/en13225889.
[43] Yi H-S, Jeong J-B, Cha S-W, Zheng C-H. Optimal component sizing of fuel cell-battery excavator based on workload. International Journal of Precision Engineering and Manufacturing-Green Technology 2018;5(1):103–10. https://doi.org/10.1007/s40684-018-0011-z.
[44] da Silva SF, et al. Aging-aware optimal power management control and component sizing of a fuel cell hybrid electric vehicle powertrain. Energy Convers Manag 2023;292. https://doi.org/10.1016/j.enconman.2023.117330.
[45] Xun Q, Murgovski N, Liu Y. Joint component sizing and energy management for fuel cell hybrid electric trucks. IEEE Trans Veh Technol 2022;71(5):4863–78. https://doi.org/10.1109/tvt.2022.3154146.
[46] Novella R, Morena JDl, Lopez-Juarez M, Nidaguila I. Effect of differential control and sizing on multi-FCS architectures for heavy-duty fuel cell vehicles. Energy Convers Manag 2023;293. https://doi.org/10.1016/j.enconman.2023.117498.
[47] Zhou S, Zhang G, Fan L, Gao J, Pei F. Scenario-oriented stacks allocation optimization for multi-stack fuel cell systems. Appl Energy 2022;308. https://doi.org/10.1016/j.apenergy.2021.118328.

[48] Zhang G, Zhou S, Gao J, Fan L, Lu Y. Stacks multi-objective allocation optimization for multi-stack fuel cell systems. Appl Energy 2023;331. https://doi.org/10.1016/j.apenergy.2022.120370.
[49] Yamchi HB, Kandidayeni M, Kelouwani S, Boulon L. The impact of stack allocation on the performance of a hybrid multi-stack fuel cell system. In: 2024 IEEE vehicle power and propulsion Conference (VPPC). IEEE; 2024. p. 1–5.
[50] Kandidayeni M, Yamachi HB, Trovao JPF. Advancing hydrogen and fuel cell technologies for sustainable aviation: challenges and future directions. In: Hydrogen and low-carbon fuels in circular Bio-economy: assessment methodologies, production technologies and sector-specific applications. Springer; 2025. p. 255–304.
[51] Tang T, et al. Energy management of fuel cell hybrid electric bus in mountainous regions: a deep reinforcement learning approach considering terrain characteristics. Energy 2024/12/01/2024;311:133313. https://doi.org/10.1016/j.energy.2024.133313.
[52] Zhao Y, Huang S, Wang X, Shi J, Yao S. Energy management with adaptive moving average filter and deep deterministic policy gradient reinforcement learning for fuel cell hybrid electric vehicles. Energy 2024/12/15/2024;312:133395. https://doi.org/10.1016/j.energy.2024.133395.
[53] Squadrito G, Maggio G, Passalacqua E, Lufrano F, Patti A. An empirical equation for polymer electrolyte fuel cell (PEFC) behaviour. J Appl Electrochem 1999;29(12):1449–55.
[54] Kandidayeni M, Soleymani M, Macias A, Trovão JP, Boulon L. Online power and efficiency estimation of a fuel cell system for adaptive energy management designs. Energy Convers Manag 2022;255:115324.
[55] Yuan X-Z, Li H, Zhang S, Martin J, Wang H. A review of polymer electrolyte membrane fuel cell durability test protocols. J Power Sources 2011;196(22):9107–16.
[56] Zhou Y, Ravey A, Péra M-C. Real-time cost-minimization power-allocating strategy via model predictive control for fuel cell hybrid electric vehicles. Energy Convers Manag 2021;229:113721.
[57] Johnson V. Battery performance models in ADVISOR. J Power Sources 2002;110(2):321–9.
[58] Bloom I, et al. An accelerated calendar and cycle life study of Li-ion cells. J Power Sources 2001;101(2):238–47.
[59] Wang J, et al. Cycle-life model for graphite-LiFePO4 cells. J Power Sources 2011;196(8):3942–8.
[60] Ebbesen S, Elbert P, Guzzella L. Battery state-of-health perceptive energy management for hybrid electric vehicles. IEEE Trans Veh Technol 2012;61(7):2893–900.
[61] PowerCellution, V stack. https://powercellgroup.com/wp-content/uploads/2022/05/v-stack-v-221.pdf. [Accessed 15 February 2025].
[62] PowerCellution, P stack. https://powercellgroup.com/wp-content/uploads/2023/10/p-stack-v-222.pdf. [Accessed 15 February 2025].
[63] Konak A, Coit DW, Smith AE. Multi-objective optimization using genetic algorithms: a tutorial. Reliab Eng Syst Saf 2006;91(9):992–1007.
[64] Macias Fernandez A, Kandidayeni M, Boulon L, Trovão JP. Effects of price range variation on optimal sizing and energy management performance of a hybrid fuel cell vehicle. IEEE Trans Energy Convers 2023;38(3):1626–38. https://doi.org/10.1109/tec.2023.3240723.
[65] Hu X, Zou C, Tang X, Liu T, Hu L. Cost-optimal energy management of hybrid electric vehicles using fuel cell/battery health-aware predictive control. IEEE Trans Power Electron 2019;35(1):382–92.
[66] Li C. The optimization of hydrogen consumption based on the controlling of charging circuit in nemo hybrid electric vehicle. Université du Québec à Trois-Rivières 2015.
[67] High-power type cells. https://www.global.toshiba/ww/products-solutions/battery/scib/product-next/product/cell/high-power.html. [Accessed 22 February 2025].
[68] Kandidayeni M, Chaoui H, Boulon L, Trovão JPF. Adaptive parameter identification of a fuel cell system for health-conscious energy management applications. IEEE Trans Intell Transport Syst 2021;23(7):7963–73.
[69] Kandidayeni M, Chaoui H, Boulon L, Kelouwani S, Trovão JP. Online system identification of a fuel cell stack with guaranteed stability for energy management applications. IEEE Trans Energy Convers 2021;36(4):2714–23.